Journal of Zhejiang University-SCIENCE A (Applied Physics & Engineering) 2024 25(6):455-469
www.jzus.zju.edu.cn; www.springer.com/journal/11582
E-mail: jzus_a@zju.edu.cn

Research Article

https://doi.org/10.1631/jzus.A2300114

Check for updates

Geometrical transition properties of vortex cavitation and associated flow-choking characteristics in poppet valves

Liang LU[1,2], Zhongdong LIANG[1], Yuming LIU[1], Zhipeng WANG[2]✉, Shohei RYU[3]

[1]*School of Mechanical Engineering, Tongji University, Shanghai 201804, China*
[2]*Frontiers Science Center for Intelligent Autonomous Systems, Tongji University, Shanghai 201210, China*
[3]*Technical Research Laboratory, Hitachi Construction Machinery Co. Ltd., Tsuchiura 300-0013, Japan*

Abstract: Poppet valves have become increasingly significant in ensuring precise digital flow rate and pressure control in hydraulic systems, necessitating a more profound understanding of the geometrical properties of cavitation in them, as well as associated flow-choking conditions. Through a comparative analysis with experimentally observed cavity images, we found that large eddy simulation (LES) turbulence modeling effectively replicates the geometrical properties of cavitation in these valves. The analysis demonstrated that cavitation is generated from vortices that result from the interaction between the notch contracta flow and the surrounding fluid structure. Variations in the internal or external vena contracta conditions result in fixed or discrete cavities, and the length-to-diameter ratio serves as a measure of the transition between internal and external vena contracta flow properties. This study establishes a threshold length-to-diameter ratio of approximately 2 for the tested poppet valves. More specifically, in notch structures with a smaller valve opening, longer sealing length, and smaller throttling angle (corresponding to a larger length-to-diameter ratio), the liquid-to-vapor transfer process is more evident than that in the reverse direction. A long-standing vapor cavity becomes fixed inside the notch, leading to a more pronounced flow-choking phenomenon. In contrast, for structures with a smaller length-to-diameter ratio, the cavitation process for discrete vapor cavities is more complete, ensuring fluid flow continuity and significantly reducing the occurrence of the flow-choking phenomenon.

Key words: Poppet valves; Vena contracta; Vortex flow; Vapor cavity; Flow-choking

1 Introduction

The poppet valve is a commonly used structure in fluid power systems, and is known for its simple and reliable control of pressure, flow rate, and flow direction. With the advent of digital control technology, the poppet valve has garnered increased attention as a crucial component for achieving high-quality flow control, particularly in the form of high-speed on-off valves, which can switch in less than 1 ms (Pan and Plummer, 2018). This new popularity is evident in its application in various systems, such as hydraulic pilot control systems for construction machinery (Wang et al., 2017) and fuel-metering systems for aero-engines (Gao et al., 2022). As system pressure steadily increases, the prevalence of wear (Lu et al., 2022) and vibration in hydraulic components has heightened, while inherent problems within the poppet valve structure are also accentuated. Chiavola et al. (2019) designed an experimental setup to test the influence of pressure fluctuations on the static characteristics of a poppet valve at different opening positions. Stosiak et al. (2023) measured the vibration of a micro relief valve with a poppet structure and proposed a modified decision-tree induction algorithm to analyze the impact of vibration on the valve. Li et al. (2021) proposed a signal analysis method based on ensemble empirical mode decomposition, which allows for a comprehensive analysis of the intensity of cavitation flow in poppet valves. To obtain information on detailed flow conditions inside valve structures, computational fluid dynamics (CFD) is commonly utilized. For the turbulence model, unsteady Reynolds-averaged Navier-Stokes (URANS) is frequently employed to

✉ Zhipeng WANG, wangzhipeng@tongji.edu.cn
Liang LU, https://orcid.org/0000-0002-9403-330X
Zhipeng WANG, https://orcid.org/0000-0003-4632-9170

Received Mar. 6, 2023; Revision accepted Aug. 16, 2023;
Crosschecked Feb. 22, 2024; Online first Apr. 2, 2024

average the transient pulsating flow and process the Reynolds stress using two-equation k-ε models, which solve the additional transport equations for the turbulent kinetic energy (k) and dissipation of turbulent energy (ε). For example, Gao et al. (2019) used the k-ε model to conduct a numerical simulation of the flow field in large-flow high-speed on-off valves. The results showed that the formation of vortices in the flow channel extracted energy from the main flow and enhanced fluid-borne noise. Based on the simulation results of the k-ε model, Filo et al. (2021) modified the geometry of the check valve, resulting in a significant reduction in pressure loss.

Furthermore, when considering throttling cavitation in various valves, its mechanism is generally estimated using the continuity equation and Bernoulli's law (Han et al., 2017; Martelli et al., 2017; Zhang et al., 2018). The notch throttling flow creates a vena contracta where the maximum velocity and the minimum pressure occur at its throat. If the pressure drops below the local vapor pressure, bubble nucleation occurs, forming visible vapor cavities. The URANS k-ε turbulence model aligns well with the averaged flow-field assumption, which is now commonly coupled with multiphase and cavitation submodels to analyze severely turbulent poppet-valve cavitation. Yuan et al. (2019a) elucidated the close connection between cavitation inception and the transition of the flow pattern in poppet valves, which contributed to understanding of flow-choking problems. With the advancements in high-speed flow visualization technology, several researchers, including the authors, have observed the presence of relatively large vapor cavities in throttling devices during experiments, and proposed that their generation might be linked to local vortices (Altimira and Fuchs, 2015; Kumagai et al., 2016; Min et al., 2020). Continuing to use the URANS k-ε turbulence model would make it quite difficult to accurately replicate the real scale of the notch cavity. Building upon this foundation, Lu et al. (2020) employed large eddy simulation (LES) as a substitute, which demonstrated notable advantages in replicating the shape of large vapor cavities. Yuan et al. (2019b, 2021, 2022) provided illustrations of the discrete cavitation-formation mechanism in poppets and discussed how variations in viscosity can lead to changes in the interaction between vortex cavitation and attached cavitation. Their work reinforced the concept of vortex cavitation. However, existing research has primarily focused on line-sealing poppet-valve structure. In reality, the flow-choking phenomenon could be even more severe in face-sealing valves. In this study, we use two representative poppet valve cases, one line-sealing and the other face-sealing, to demonstrate the discrepancy between discrete and fixed vortices, along with the associated discrete and fixed vapor cavities, based on the external and internal flow vena contracta theory. A critical index of length-to-diameter ratio, constituted by notch configural parameters, is proposed to measure the state-transition process of vena contracta flow. The flow-choking phenomenon is explained from the perspective of vortex-cavitation mass transfer. Such specific delineation of poppet-valve cavitation may be helpful in furthering anti-cavitation design of valve structures.

2 Experimental approach

2.1 Parameter design

As basic fluid mechanics theory suggests (Finnemore and Franzini, 2002), the thin-wall-orifice structural characteristic exists when the thickness (length) of a wall is very small relative to the size of the opening (diameter). In other words, when the length-to-diameter ratio of an orifice is quite small, it produces a vena contracta downstream of the orifice outlet. In contrast, the thick-wall-orifice structural characteristic is present if the length-to-diameter ratio is more than 2, resulting in a vena contracta inside the orifice. Since the vena-contracta flow velocity is significantly higher than the surrounding flow, friction shear occurs, leading to the formation of two distinct types of local vortex. For the thick-wall orifice shown in Fig. 1a, the vena contracta occurs inside the orifice, and the interaction between the expansion flow and orifice wall generates fixed vortices. In the case of the thin-wall

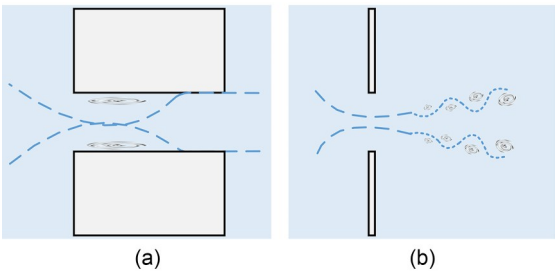

Fig. 1 Two types of flow vena contracta: (a) internal vena contracta for the thick-wall orifice; (b) external vena contracta for the thin-wall orifice

orifice shown in Fig. 1b, the vena contracta occurs outside the orifice. Here, the interaction between the expansion flow and surrounding fluid leads to the formation of a series of discrete and traveling vortices, independent of the influence of the orifice wall.

The theoretical definition of the orifice structure in fluid mechanics could be applied to the poppet-valve situation under examination. As shown in Fig. 2, the valve opening L_x, sealing length L_s, and throttling angle α are defined. The rectangle *A*-*B*-*C*-*D* represents the cross-section of the annular throttling domain, which could also be considered as a typical hydrodynamic orifice structure. As mentioned above, the flow characteristics of the thin-wall and thick-wall orifices would result in significant differences in the vena contracta and related vapor conditions. To establish a reasonable measurement basis, it is first necessary to determine the length-to-diameter ratio. As shown in Fig. 2, due to the identical flow properties of all sections such as *A*-*B*-*C*-*D*, it is reasonable to consider *A*-*B*-*C*-*D* as the rotationally symmetric cross-section of a certain tapered cylindrical domain, with the length of *A*-*B* or *D*-*C* as "diameter" and the length of *A*-*D* or *B*-*C* as "length". Thus, the parameter "length-to-diameter ratio" of the 2D flow domain *A*-*B*-*C*-*D* could be defined as the ratio of length *A*-*D* to *A*-*B*, which can be expressed by:

$$R_a = \frac{L_s}{L_x \sin\alpha}. \tag{1}$$

2.2 Experimental system

To observe the cavitation near the notch of the poppet valve, we designed a comprehensive visualization experiment system, as shown in Fig. 2. The pump station provided the necessary flow circulation for the test valve, with a parallel relief valve installed to modify the inlet pressure and an in-series throttle valve to adjust the outlet pressure. The flowmeter was positioned downstream of the pump to record the test flow rate, while essential accessories such as a safety valve and filter were included to ensure smooth functioning of the entire system. To conduct the test procedures, we equipped the system with a high-speed camera and two pressure gauges. The camera was capable of capturing a maximum of 600 thousand images per second, and had a xenon lamp to provide sufficient light intensity. Correspondingly, the test valve body was constructed using transparent polymethyl methacrylate (PMMA) material with a refractive index of 1.49, transmittance of 92, and haze of 1.5, to meet the visualization requirements. The pressure gauges were positioned close to the test valve inlet and outlet, taking into account the need to minimize the simulation domain. Moreover, the latter section of the poppet was designed in a threaded shape with a graduated disc at the end, allowing for precise adjustment and measurement of the throttle opening.

The extent of cavitation or potential of its occurrence could be described by a dimensionless number known as the cavitation number, as shown in Eq. (2).

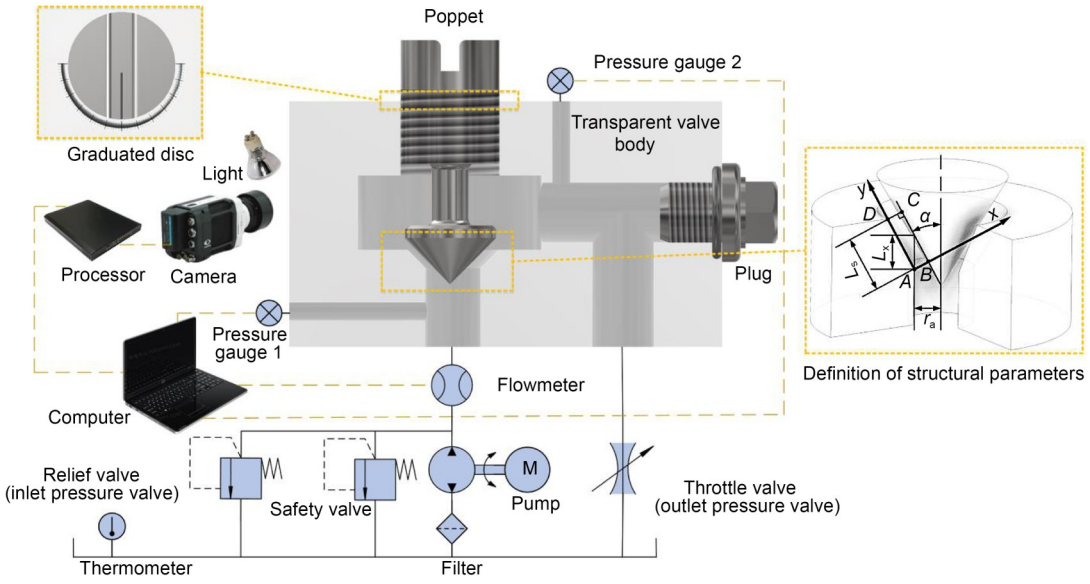

Fig. 2 Schematic of the experimental system including definition of structural parameters

$$\sigma=\frac{p_{\text{out}}-p_{\text{v}}}{p_{\text{in}}-p_{\text{out}}}, \tag{2}$$

where p_{in} and p_{out} represent the inlet and outlet pressures of the test poppet valve, respectively, while p_{v} denotes the vapor pressure under specific temperature conditions. To ensure the safety of the PMMA material, the experiment was conducted under low-pressure conditions, and p_{in} was maintained constant at 3.0 MPa. As the occurrence of cavitation is not dependent on pressure but mainly related to the σ (Brennen, 2014), conducting experiments under low-pressure conditions allowed us to effectively observe the cavitation phenomenon. We used L-HM 46 hydraulic oil, a mineral oil widely used in fluid power transmission and control systems. All the experimental parameters involved in this study are listed in Table 1. Additionally, we analyzed more structural parameters through numerical calculations.

Table 1 Experimental parameters

	Parameter	Value
Physical	ρ_{l} (kg/m^3)	889
	μ_{l} (kg/(m·s))	0.045
	ρ_{v} (kg/m^3)	0.55
	μ_{v} (kg/(m·s))	1.34×10^{-5}
	p_{v} (Pa)	10
Structural	Inlet radius, r_{a} (mm)	4
	L_{s} (mm)	0.00, 2.00, 4.00, 6.00
	L_{x} (mm)	1.00
	α (°)	30, 45, 60
Flow	p_{in} (MPa)	3.0
	p_{out} (MPa)	⩾0.15
	Temperature (°C)	40±1

3 Numerical approach

3.1 Grid generation

The simulation flow domain was constructed based on the test-valve structure and boundary-pressure metering conditions, corresponding to Fig. 2. Although the outlet flow channel was not perfectly circular, the 3D flow domain could be generally treated as axisymmetric. Therefore, the simulation flow domain could be simplified to a 2D cross-section, as shown in the area surrounded by thick solid lines in Fig. 3a.

As mentioned in Section 1, the LES turbulence model has demonstrated promising results in simulating cavitation generated by vortices, thus making it applicable in this study. For LES, we employed a high-quality structured grid to ensure accuracy and efficiency of calculation. Due to the limited flexibility of structural grids, a partitioned division approach was required. As shown in Fig. 3b, the computational domain consisted of the inlet region, valve-notch region, and outlet region. To ensure that each region had a quadrilateral structure, six quadrilateral blocks were further segmented, as illustrated in Fig. 3c. It is necessary to clarify that block 3 did not exist for the

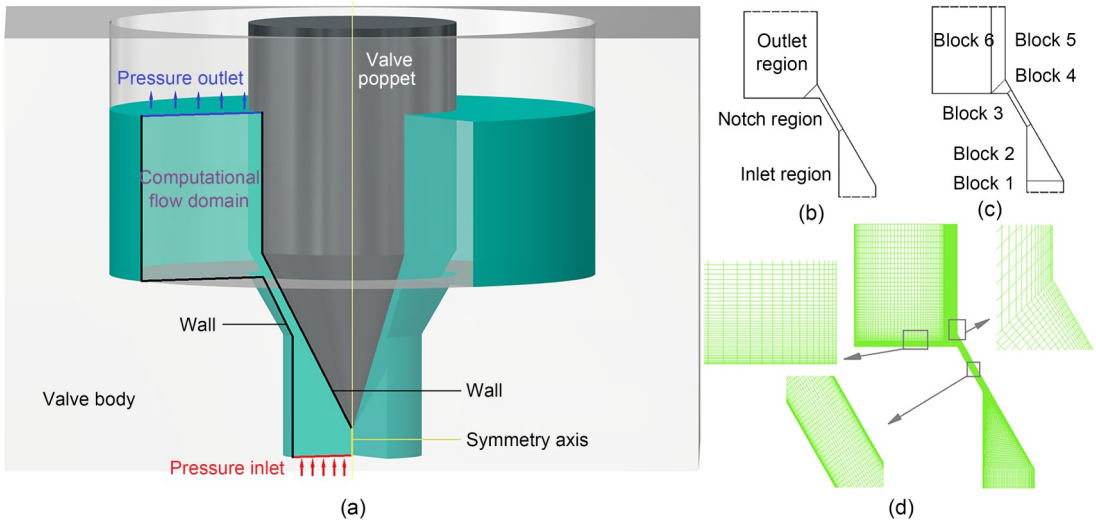

Fig. 3 Simplification and gridding of the computational fluid domain: (a) simplified computational flow domain; (b) region partition; (c) blocking; (d) gridding

line-sealing poppet valve. The near-wall area of the grid was refined, with the wall distance set at 1 μm and the grid growth rate at 1.05. This ensured that the dimensionless wall distance y^+ of the grid was strictly less than 1, placing the first grid cell within the viscous sublayer. As a result, the wall shear stress could be accurately calculated directly from the velocities in the first cell without using a wall function. In addition, to thoroughly analyze the cavitation phenomenon in the notch region, a large number of grid nodes were set up in blocks 3 and 4, as shown in Fig. 3d.

3.2 Governing equations

3.2.1 Multiphase model

In fluid power transmission and control systems, the average sound velocity of hydraulic oil is approximately 1300 m/s, and the maximum flow velocity typically does not exceed 200 m/s. Consequently, in this study the fluid was considered to be incompressible. Assuming that the current flow is characterized by homogeneous multiphase flow with phases moving at the same velocity, the mixture model (Manninen et al., 1996), a simplified multiphase model, can be employed:

$$\rho_{\mathrm{m}}=\rho_{\mathrm{v}}\alpha_{\mathrm{v}}+\rho_{\mathrm{l}}(1-\alpha_{\mathrm{v}}), \tag{3}$$

$$\mu_{\mathrm{m}}=\mu_{\mathrm{v}}\alpha_{\mathrm{v}}+\mu_{\mathrm{l}}(1-\alpha_{\mathrm{v}}), \tag{4}$$

where α_{v} represents the volume fraction number of vapor, ρ_{m}, ρ_{l}, and ρ_{v} are the densities of the mixture, liquid, and vapor, respectively, and μ_{m}, μ_{l}, and μ_{v} are the dynamic viscosities of the mixture, liquid, and vapor, respectively.

3.2.2 Turbulence model

Generally, turbulence is characterized by vortices with a wide range of lengths and time scales. Implicit LES resolves large energy-containing eddies at grid nodes, while smaller and isotropic eddies are handled by the sub-grid scale turbulence model to close the governing equations. The LES equations are derived by applying a second-order commuting filter to the incompressible Navier-Stokes equation and continuity equation (Ghosal and Moin, 1995):

$$\frac{\partial\rho_{\mathrm{m}}}{\partial t}+\frac{\partial\left(\rho_{\mathrm{m}}\bar{u}_j\right)}{\partial x_j}=0, \tag{5}$$

$$\frac{\partial(\rho_{\mathrm{m}}\bar{u}_i)}{\partial t}+\frac{\partial\left(\rho_{\mathrm{m}}\bar{u}_i\bar{u}_j\right)}{\partial x_j}=-\frac{\partial\bar{p}}{\partial x_i}+\frac{\partial}{\partial x_j}\left(\mu_{\mathrm{m}}\frac{\partial\bar{u}_i}{\partial x_j}\right)-\frac{\partial\tau_{ij}}{\partial x_j}, \tag{6}$$

where t is the time, p is the pressure, u is the velocity, x is the Cartesian coordinate, the subscripts (i, j, k) denote the directions of the Cartesian coordinates, and $\boldsymbol{\tau}_{ij}$ denotes the sub-grid scale stress (SGS). The complete form of the momentum equations for 2D axisymmetric geometries are listed in Section S1 of the electronic supplementary materials (ESM).

The Boussinesq hypothesis (Hinze, 1975) was employed to model the SGS tensor, which was generated by the filtering operation in LES:

$$\boldsymbol{\tau}_{ij}=-2\mu_{\mathrm{t}}\boldsymbol{S}_{ij}, \tag{7}$$

where μ_{t} represents the eddy viscosity and $\boldsymbol{S}_{ij}$ denotes the rate-of-strain tensor for the resolved scale. It should be noted that the SGS tensor also contained isotropic components, which were added to the filtered static pressure term without the need for additional modeling. We used the wall-adapting local eddy viscosity (WALE) model (Nicoud and Ducros, 1999) to further model the eddy viscosity, and its complete formulas are provided in Section S2 of the ESM.

3.2.3 Cavitation model

Cavitation model suggests that cavitation is formed by the development of nuclei bubbles in the low-pressure zone of the liquid. We used this model to simulate the process of liquid evaporating under lower local pressure and condensing under greater local pressure, in comparison to the vapor pressure at the local temperature. Common cavitation models include the full cavitation model (Singhal et al., 2002), the Schnerr-Sauer model (Schnerr and Sauer, 2001), and the Zwart-Gerber-Belamri model (Zwart et al., 2004). The full cavitation model considers all the first-order effects, including non-condensable bubbles, bubble dynamics, phase transitions, and turbulent pressure fluctuations. However, it is numerically unstable and cannot be coupled with the LES. The remaining two models differ significantly from the first; they are robust and converge quickly. The Schnerr-Sauer model (Schnerr and Sauer, 2001) uses vapor volume fraction for two-phase modeling; this closely corresponds to our grayscale experimental vapor images, making it the preferred choice for this study:

$$\frac{\partial(\rho_v\alpha_v)}{\partial t}+\frac{\partial\left(\rho_v\alpha_v u_j\right)}{\partial x_j}=\dot{m}^+-\dot{m}^-, \tag{8}$$

where the source term $\dot{m}^+$ represents evaporation and $\dot{m}^-$ represents condensation. The complete formulas of the Schnerr-Sauer model are provided in Section S3 of the ESM.

3.3 Numerical solution

To achieve more accurate numerical results, we adopted the coupled calculation method, which requires sacrificing some computational time and central processing unit (CPU) resources. The actual calculations were conducted using Ansys Fluent, and the detailed solution methods can be found in Section S4 of the ESM.

The physical parameters for the numerical calculations were kept identical to those in the experiment. Pressure inlet and pressure outlet were used as boundary conditions. The inlet pressure remained constant at 3.0 MPa, while the outlet pressure varied based on specific operating conditions. To approximate the unsteadiness of cavitation, we used transient calculation, with a time step size set to 10^{-6} s, and each case contained more than 4000 time steps. The calculation was considered to have converged when the residuals of velocities were below 10^{-6} and the residual of the vapor volume fraction was below 10^{-4}.

For grid independence verification, we generated a series of grids with increasing cell numbers, denoted as Grid 1, Grid 2, and Grid 3. The grid convergence index (GCI), based on generalized Richardson extrapolation (Roache, 1998), was used to estimate the grid convergence of the solution and provide an error band. The complete grid refinement method and GCI calculation formulas are listed in Section S5 of the ESM. The time-averaged flow rates under the same pressure and notch-structure conditions were used as the characterization index for grid-independence verification. As shown in Table 2, further refining the grid based on Grid 2 only resulted in a maximum of 0.32% change in solutions. In other words, using Grid 2 for the calculations introduced a maximum error of 0.32%, and it was not necessary to continue refining the grid. Ultimately, we chose to use grids with identical spacing to Grid 2 for the calculations in this study.

To demonstrate the effectiveness of the numerical modeling, the time-averaged flow rate is compared between simulation and experiment under different back pressure conditions, for both line-sealing and face-sealing poppet valves, as shown in Fig. 4. It can be observed that the relative error is no more than 4%, which is within an acceptable range.

Table 2 GCI of three grid conditions (L_s=4.00 mm, L_x=0.50 mm, α=30°, p_{out}=0.20 MPa)

Type	Cell number ($\times10^6$)	Time-averaged flow rate (L/min)	GCI (%)
Grid 1	0.075	21.7187	2.06
Grid 2	0.300	21.4160	0.32
Grid 3	1.200	21.3687	0.05

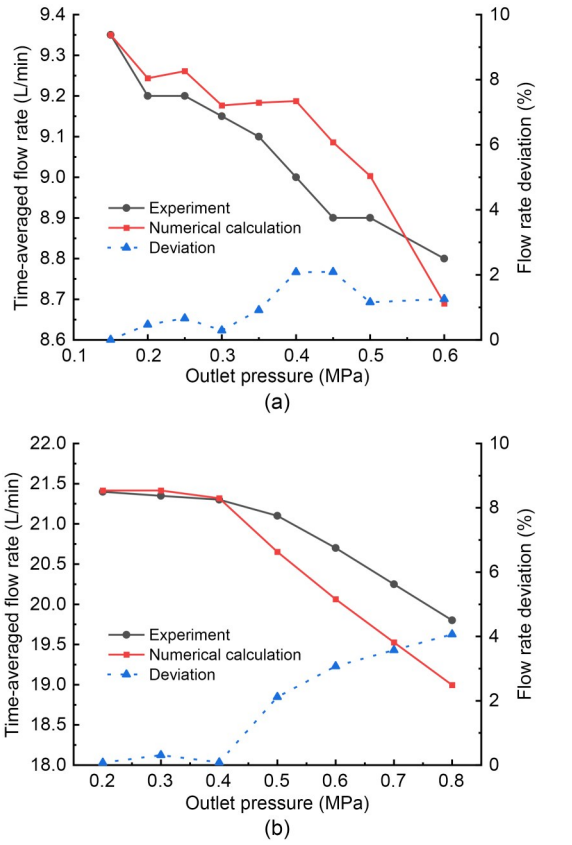

Fig. 4 Comparison between the experimental and numerical time-averaged flow rates: (a) line-sealing (L_s=0.00 mm, L_x=0.25 mm, α=30°); (b) face-sealing (L_s=4.00 mm, L_x=0.50 mm, α=30°)

4 Results and discussion

4.1 Mechanism analysis of flow-vortex-produced vapor cavities

Using two typical structures as examples (face-sealing and line-sealing poppet valves), we will

discuss two distinct causes of cavitation. We must point out that two-phase flow is assumed to be homogeneous in the mixture model. Consequently, an independent vapor cavity with a clear vapor-liquid interface cannot be explicitly presented using the proposed modeling approach; a vapor fraction number of 0.6 is used as the isosurface threshold to divide the vapor fraction gradient into two directions (marked with different colors), allowing for a better revelation of cavitation geometry. Fig. 5 illustrates the detailed formation mechanism of the fixed vapor cavity that occurs in the face-sealing poppet valve. As shown in Figs. 5a and 5b, under the proposed conditions, the notch cavitation exhibits a fixed vapor cavity near the valve seat wall, while a few scattered vapor cavities appear downstream. The region with lower pressure than vapor pressure is concentrated in the same area, as indicated in Fig. 5c. This local low pressure appears to be generated by local vortices formed by the interaction of the internal flow vena contracta and the valve seat wall, as evident from the flow streamline distributions displayed in Figs. 5d and 5e. In comparison to Fig. 1a, one can see that the internal flow vena contracta only occurs near the valve seat under the proposed conditions, as there is no sharp edge present on the poppet side. Moreover, the essence of the cavitation process lies in the transform between the two phases. As shown in Fig. 5f, near the notch inlet, the liquid phase transforms into the vapor phase, while near the notch outlet, the vapor phase transforms back into the liquid phase. The process of liquid-to-vapor transfer is more dominant, resulting in the persistence of a fixed vapor cavity inside the notch.

Fig. 6 illustrates geometrical properties of the cavity with increasing outlet pressure (from a certain low level), with the inlet pressure maintained at 3.0 MPa and the same face-sealing poppet-valve conditions. It is clear that the cavity region consistently corresponds to the vortex region. As the outlet pressure increases, the notch flow velocity decreases, leading to a gradual reduction in the cavity scale, while the fixed shape of the cavity remains unchanged.

Regarding the line-sealing poppet valve, Fig. 7 illustrates the detailed formation mechanism of the

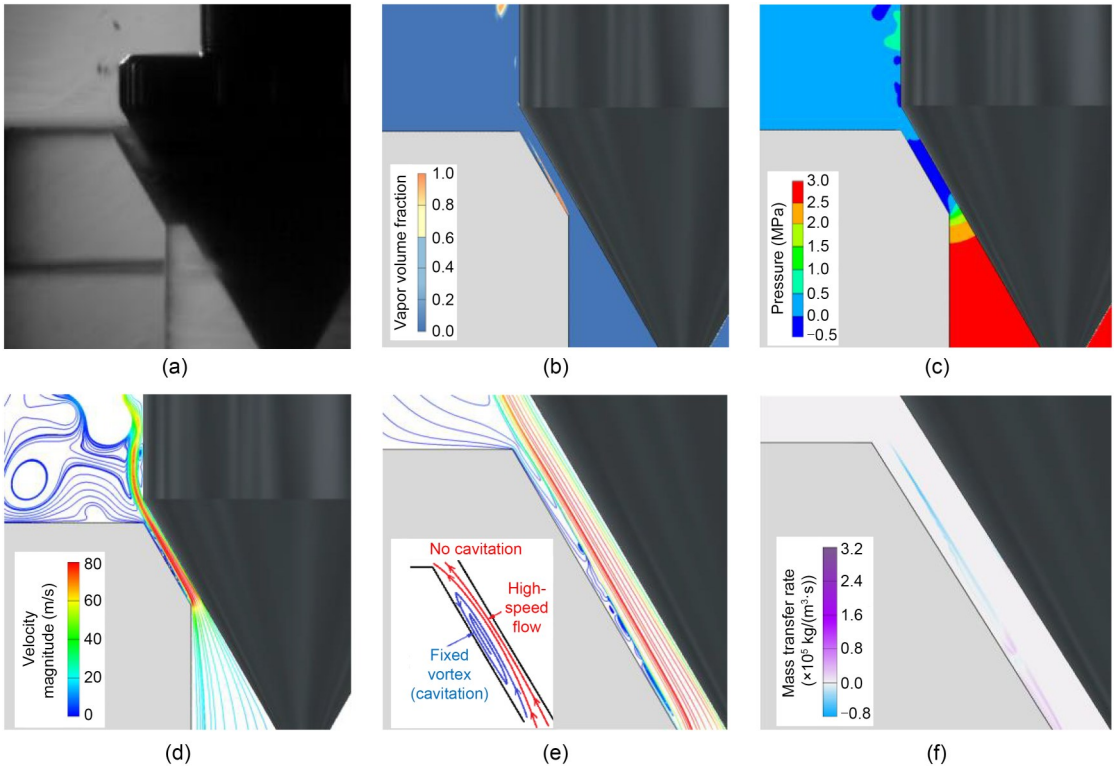

Fig. 5 Illustration of the formation of the fixed vapor cavity in a face-sealing poppet valve: (a) cavity image from experiment; (b) simulation result for cavity isosurface; (c) notch pressure distribution; (d) notch streamline distribution; (e) fixed vortex generated by internal flow vena contracta; (f) cavitation mass transfer (L_s=4.00 mm, L_x=1.00 mm, α=30°, p_{out}=0.20 MPa). References to color refer to the online version of this figure

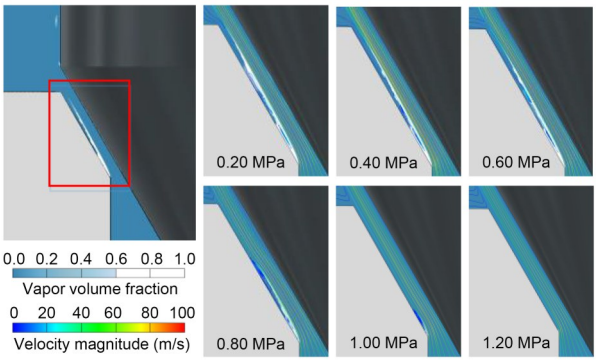

Fig. 6 Geometrical properties of the cavity with increasing outlet pressure in a face-sealing poppet valve (L_s=4.00 mm, L_x=1.00 mm, α=30°). References to color refer to the online version of this figure

discrete vapor cavities. As shown in Figs. 7a and 7b, the discrete vapor cavities are distributed downstream of the notch, with hardly any fixed vapor cavity appearing. The region of lower pressure than vapor pressure is distributed downstream of the notch, as indicated in Fig. 7c. This phenomenon deviates from traditional interpretations of cavitating bubble flow that adhere to Bernoulli's law and the continuity equation. As shown in Figs. 7d and 7e, discrete vapor cavities do not occur inside the throat of the vena contracta, which is expected to have the lowest pressure and the maximum flow speed. Instead, these discrete vapor cavities appear in the submerged jet-shear vortices formed by the interaction between the high-speed external vena contracta flow and the relatively static surrounding fluid. Correspondingly, the mass transfer processes occur at the same time in the shearing vortex regions. In each vortex core, the liquid phase transfers to the vapor phase, while at the edge of the vortex, the vapor phase transfers back to the liquid phase, as shown in Fig. 7f.

Fig. 8 illustrates the geometrical properties of the cavities with increasing outlet pressure (from a certain low level) with the inlet pressure maintained at 3.0 MPa under the set line-sealing poppet valve conditions. It is evident that the discreteness of the vapor cavities remains consistent with different outlet pressures, and no fixed cavity exists. As the outlet pressure decreases, the number and scale of cavities increase, and individual vapor cavities even merge into vapor clusters.

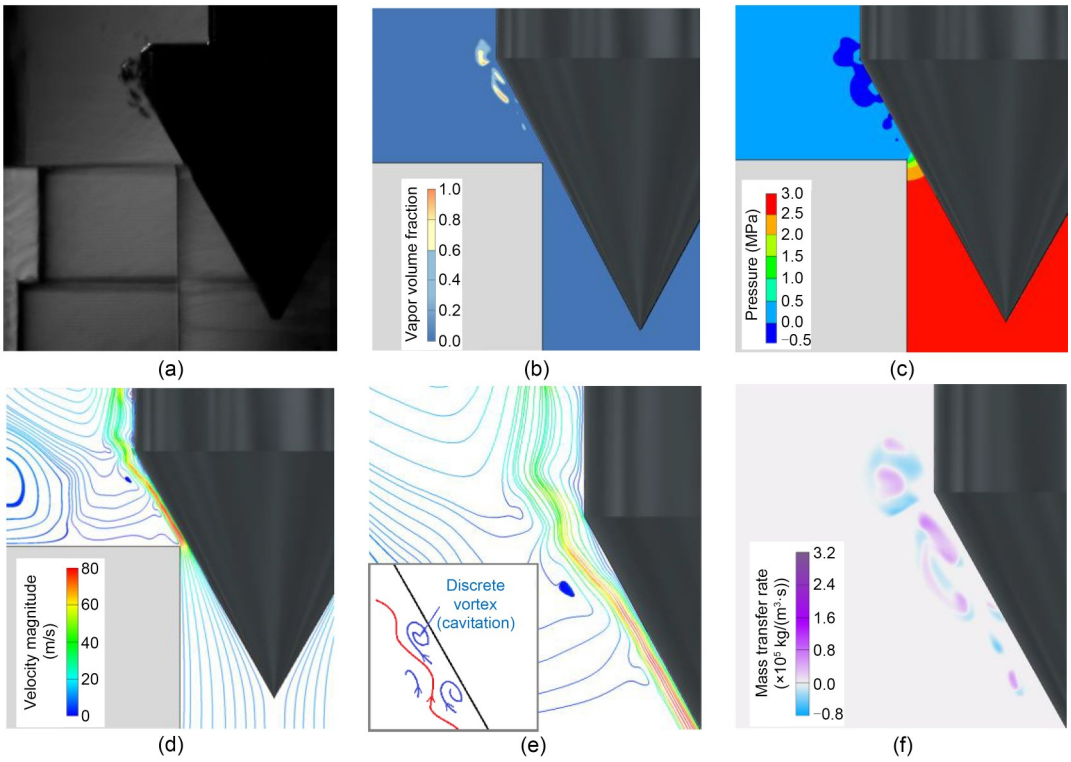

Fig. 7 Illustration of the formation of discrete vapor cavities in a line-sealing poppet valve: (a) cavity image from experiment; (b) simulation result for cavity isosurface; (c) notch pressure distribution; (d) notch streamline distribution; (e) discrete vortex generated by internal flow vena contracta; (f) cavitation mass transfer (L_s=0.00 mm, L_x=0.50 mm, α=30°, p_{out}=0.20 MPa). References to color refer to the online version of this figure

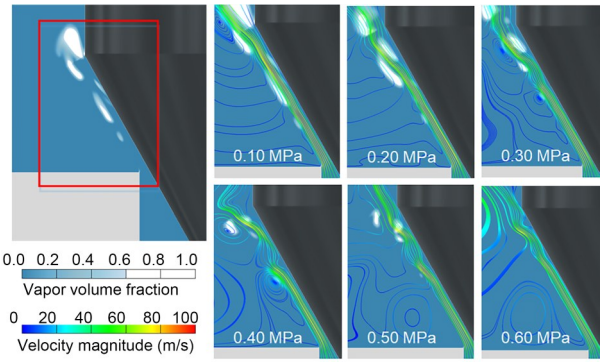

Fig. 8 Geometrical properties of the cavities with increasing outlet pressure in a line-sealing poppet valve (L_s=0.00 mm, L_x=1.00 mm, α=30°). References to color refer to the online version of this figure

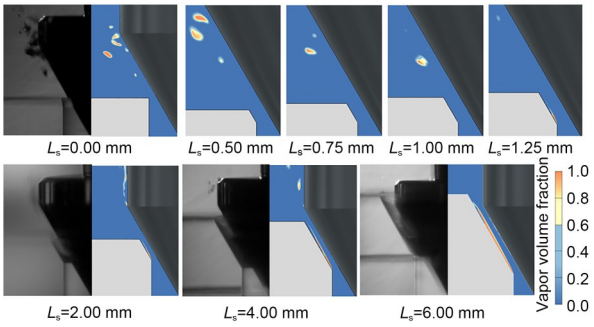

Fig. 9 Geometrical properties of the cavity with changing L_s (L_x=1.00 mm, α=30°, p_{out}=0.20 MPa). References to color refer to the online version of this figure

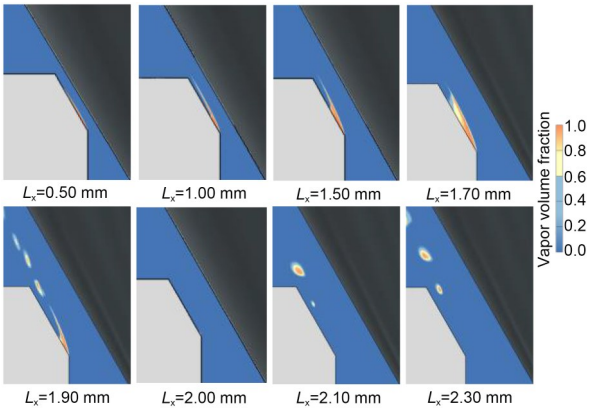

Fig. 10 Geometrical properties of the cavity as L_x changes (L_s=2.00 mm, α=30°, p_{out}=0.20 MPa). References to color refer to the online version of this figure

It can be concluded that both the fixed vapor cavities produced in face-sealing poppet valves and the discrete vapor cavities produced in line-sealing poppet valves are formed by flow vortices. The difference in physical properties between the internal vena contracta of the face-sealing orifice structure and the external vena contracta of the line-sealing orifice structure leads to distinct shape and distribution features of cavitation in these two patterns. Additionally, altering the pressure only changes the cavity scale, not the shape or distribution features.

4.2 Effects of the vena contracta on cavity features

The properties of the vena contracta significantly influence the properties of cavitation. R_a serves as a reflection of the vena contracta properties, making it easier to identify the parameters that play a significant role in notch cavitation, as shown in Eq. (1). It should be noted that cavitation is a transient process. However, in this section, the primary focus is on the types of cavitation in various structures, while the transient behavior of cavitation is analyzed later. To accurately identify cavitation types, the figures showing the time step with the largest fixed cavity scale at the valve notch were selected, as shown in Figs. 9–11. For the cases without a fixed cavity at the valve notch, the figures showing the time step with the most vapor cavities were selected.

4.2.1 Sealing length, L_s

The transition of cavity geometrical properties with changes in the sealing length under representative pressure conditions is shown in Fig. 9; L_x and α are constant. One can see that when the L_s is equal to or less than 1.00 mm, no fixed cavity appears near the valve seat, but discrete vapor cavities are present downstream. As L_s slightly increases, for example, at 1.25 mm, a minor but distinct fixed cavity occurs near the seat wall. With further increases in L_s, the fixed cavity scale becomes larger. This could be explained by the fact that as L_s increases, R_a increases, making the poppet notch more similar to a thick-wall orifice. This structure creates an internal vena contracta and generates fixed vortices and a fixed vapor cavity.

4.2.2 Valve opening, L_x

The transition of cavity geometrical properties with changes in the L_x under representative pressure conditions is shown in Fig. 10. It can be observed that when L_x is less than 2.00 mm, a fixed cavity exists near the valve-seat wall. As L_x increases, the fixed cavity tends to move away from the wall. When L_x increases to nearly 2.00 mm, discrete vapor cavities

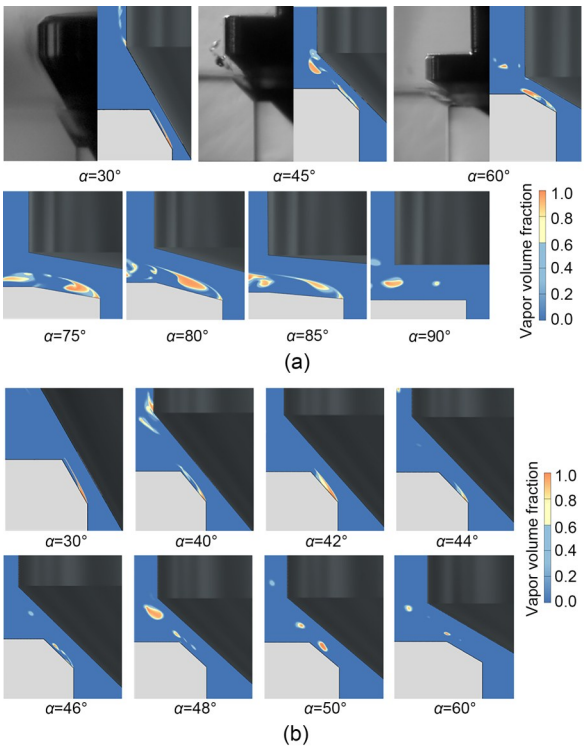

Fig. 11 Geometrical properties of the cavity as α changes (L_x=1.00 mm, p_{out}=0.20 MPa): (a) with L_s=2.00 mm; (b) with L_s=1.50 mm. References to color refer to the online version of this figure

gradually appear behind the fixed cavity. Once L_x reaches 2.00 mm, no fixed cavity exists and only discrete vapor cavities are present. The underlying mechanism remains the same. As the L_x increases, R_a drops, making the poppet notch more similar to a thin-wall orifice. This structure creates an external vena contracta and generates discrete vortices and vapor cavities.

4.2.3 Throttle angle, α

Fig. 11a shows the transition of cavity geometrical properties with changes in the α under representative pressure conditions. It is clear that when α is between 30° and 90°, a fixed cavity exists near the valve-seat wall. As α approaches 90°, the area of the fixed cavity that nearly touches the valve seat decreases, and more discrete vapor cavities appear downstream. Once α reaches 90°, no fixed cavity exists and only discrete vapor cavities are present. The turning point from a fixed to a discrete cavity occurs at the extreme angle of 90°. To provide further evidence, an additional case with a different sealing length is illustrated in Fig. 11b. In this case, a similar transition process occurs, with the cavity geometrical property changing point at an angle of 48°. The underlying mechanism remains the same. As α increases, R_a drops, making the poppet notch more similar to a thin-wall orifice. This structure creates an external vena contracta and generates discrete vortices and vapor cavities.

Based on the above discussion, it can be deduced that a specific R_a exists to differentiate between thick-wall-orifice and thin-wall-orifice structures and internal and external vena contracta flow conditions, as well as the geometrical properties of the fixed cavity and discrete vapor cavities. The estimated R_a thresholds shown in Figs. 9–11 are summarized in Table 3. It is evident that the R_a thresholds are nearly the same (approximately 2), which aligns well with classical flow dynamic theory.

Table 3 Estimation of R_a thresholds

Independent variable	L_s (mm)	L_x (mm)	α (°)	Threshold of R_a
L_s	1.00	1.00	30	2.00
L_x	2.00	2.00	30	2.00
α	2.00	1.00	90	2.00
	1.50	1.00	48	2.02

Further, we can calculate the absolute value of partial derivatives of R_a with respect to each of the three parameters (L_s, L_x, and α) in Eq. (1):

$$\begin{cases} \left|\dfrac{\partial R_a}{\partial L_s}\right| = \dfrac{1}{L_x \sin\alpha} = \dfrac{R_a}{L_s}, \\ \left|\dfrac{\partial R_a}{\partial L_x}\right| = \dfrac{L_s}{L_x^2 \sin\alpha} = \dfrac{R_a}{L_x}, \\ \left|\dfrac{\partial R_a}{\partial \alpha}\right| = \dfrac{L_s \cos\alpha}{L_x \sin^2\alpha} = \dfrac{R_a}{\tan\alpha}. \end{cases} \tag{9}$$

Here, when L_s is equal to L_x, equal amplitude changes in L_s and L_x have a similar effect on R_a. When L_s is not equal to L_x, changing the smaller of the two parameters is more efficient in influencing R_a. Additionally, when α is relatively small, for example α=30° (tanα=0.577), changing α can effectively alter R_a. However, tanα increases sharply as α increases. When α=90°, tanα approaches positive infinity, and the rate of change of R_a with respect to α approaches zero. In other words, changing α is only effective if α is relatively small. To eliminate the fixed vapor cavity and to relieve flow-choking, R_a should be decreased. In

engineering applications, the L_x is closely related to the flow rate and generally cannot be changed. Therefore, when the α is relatively small, it can be increased to achieve the desired effect. In other cases, it would be preferable to reduce the L_s.

4.3 Specific explanations for flow-choking involving vapor-cavity formation

The flow-choking phenomenon in control valves is widely recognized in various industrial applications (Tamburrano et al., 2019; Iravani and Toghraie, 2020; Hao et al., 2022). The early consensus from an industrial perspective is that when flow-choking occurs, the pressure at the valve orifice throat can be regarded as the vapor pressure or even as zero (for hydraulic oil situations). Consequently, the flow-rate formula can still be derived from the continuity equation and Bernoulli's law, considering only the flow section from the orifice inlet to the throat. Lu et al. (2009) proposed a revised flow-rate formula based on statistics. However, most related research is based on parametric statistics. The insights into cavity geometrical properties in this study could provide additional information about cavitation-induced flow-choking.

Fig. 12 displays the transient process of cavitation in a face-sealing poppet-valve notch, with T_0 representing the starting time of the process. The cavity scale expands and shrinks along the length direction while remaining fixed at notch and not tending to collapse. This expansion and shrinking process might be attributable to the cavitation surge phenomenon, as

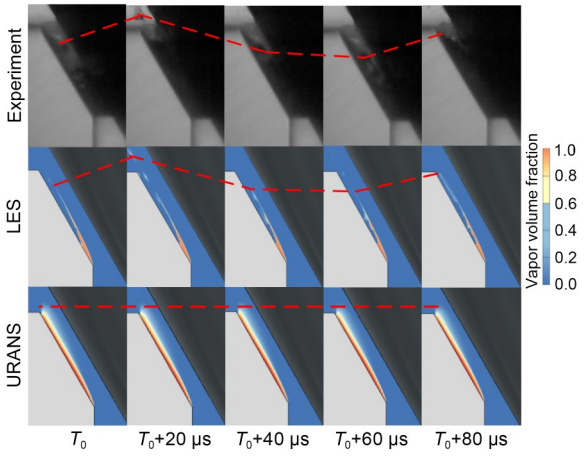

Fig. 12 Transient process of cavitation in a face-sealing poppet-valve notch (L_s=4.00 mm, L_x=1.50 mm, α=30°, p_{out}=0.20 MPa). References to color refer to the online version of this figure

discussed in our previous research on spool-valve cavitation (Lu et al., 2020). It is worth noting that the fixed cavity can persist all the time, which may be due to the stronger mass-transfer process from liquid to vapor, as shown in Fig. 5f. Since the cavity scale increases with the inlet and outlet pressure difference, as shown in Fig. 6, the effective flow area in the notch is reduced, thereby partly offsetting the increasing effect of the pressure difference on the flow rate. The process may reach a balance (Lu et al., 2022), resulting in the time-averaged flow rate hardly changing with increasing pressure difference, which leads to flow-choking.

Fig. 13 shows the transient process of cavitation in a line-sealing poppet-valve notch. No fixed cavity is visible, but some individual traveling vapor cavities are traced going through a complete cavitation process, starting from inception and ending in collapse. The two-phase mass transfer is continuous throughout the process. In these conditions, the flow continuity is not broken, and the single-phase flow-rate equation remains applicable. Therefore, it can be inferred that the flow-choking phenomenon would not be obvious in line-sealing poppet valves. More specifically, it would not be obvious in poppet-valve notches with thin-wall orifices.

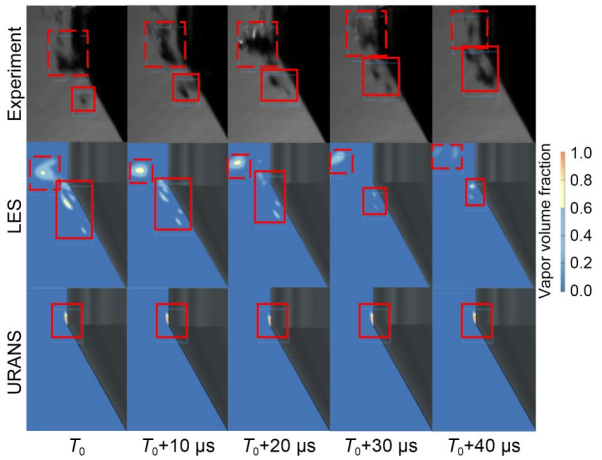

Fig. 13 Transient process of cavitation in a line-sealing poppet-valve notch (L_s=0.00 mm, L_x=0.50 mm, α=30°, p_{out}=0.20 MPa). References to color refer to the online version of this figure

As mentioned above, the flow-choking phenomenon is closely related to the geometrical features of the poppet-valve notch. Since R_a is proven to be suitable for measuring cavity geometrical features and

the transition of the vena contracta type, it could also serve as a good indicator of the extent of flow-choking. The relationships between the time-averaged flow rate and the average velocity from pressure difference (Δp), with different L_s, L_x, and α, are presented in Fig. 14. It is not difficult to conclude that when R_a is quite small, the flow-rate curves are almost straight.

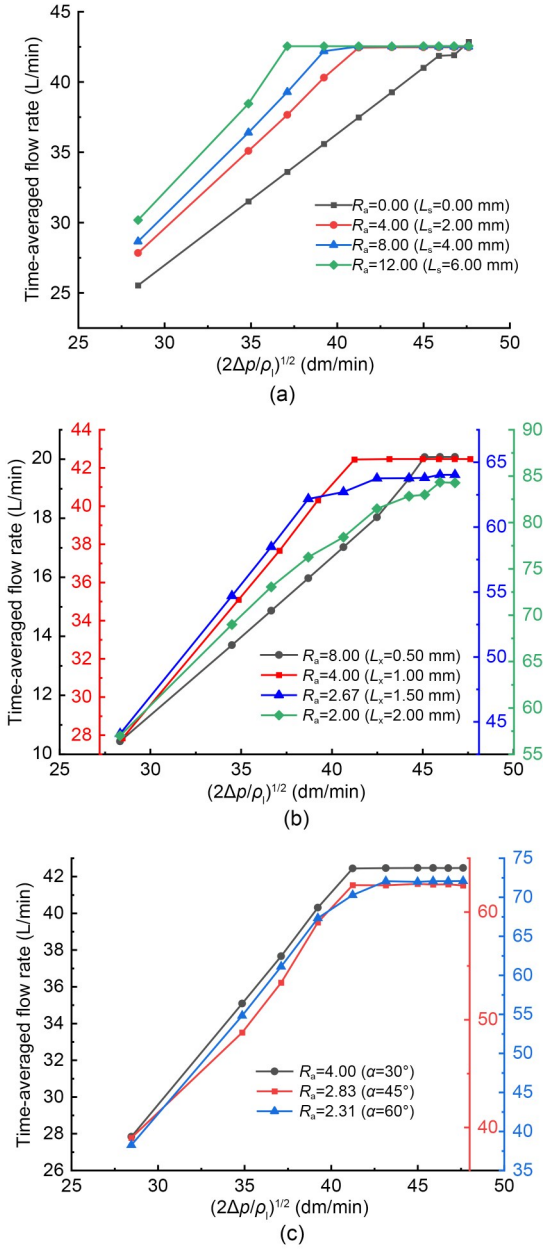

Fig. 14 Time-averaged flow rate versus the average velocity from pressure difference under different R_a conditions: (a) with different L_s (L_x=1.00 mm, α=30°); (b) with different L_x (L_s=2.00 mm, α=30°); (c) with different α (L_s=2.00 mm, L_x=1.00 mm). References to color refer to the online version of this figure

As R_a increases, a turning point appears on the flow-rate curve, and after the turning point, the curve becomes horizontal, indicating flow-choking. Specifically, a larger R_a value leads to an earlier turning point, representing more severe flow-choking.

4.4 Further explanation of the numerical model

To demonstrate the superior effectiveness of the LES model over the URANS model, we conducted a comparison of the notch cavitation geometry between the experimental images and the numerical results from the LES and URANS (k-ε) models. As shown in Fig. 12, the results obtained from LES successfully replicated the scale surging of the fixed vapor cavity, and the variation pattern of the vapor-cavity scale for each cycle aligned closely with the experimental results. As shown in Fig. 13, although complete consistency between the LES results and the experimental results was hindered by the randomness in the formation of discrete cavities, it still effectively replicated the entire cycle of discrete cavities from inception to collapse. Regarding the URANS results, although they were derived from transient calculations, the vapor-cavity geometry in each time step remained essentially unchanged, resulting in a failure to replicate the dynamic process of cavitation. For the face-sealing structure, the URANS results could only give the approximate cavitation range and could not replicate the geometrical details of the fixed cavity. In the line-sealing structure, the discrete cavities could not be replicated.

In this study, LES was applied to an axisymmetric 2D model which was designed for 3D calculation. The main consideration was to reduce the computational cost. Regarding alternative models that also reduce computational cost, as mentioned above, URANS cannot accurately replicate the cavitation at the poppet-valve notch. Although hybrid URANS-LES models can reduce the grid cell numbers on the 2D cross-section by 3–4 times for the proposed structure, because the constraints of increased resolution near the wall can be relaxed, applying these models to a 3D structure will result in overall grid cell numbers increasing by more than 10 times for such a structure. Therefore, the calculation cost would not be reduced. In this study, the geometric structure is rotationally symmetrical, and there is no significant circumferential flow. The 2D LES provides results that are very consistent with the experimental data, making it the

best choice in terms of the cost-benefit measure. In fact, for certain structures under certain conditions, 2D LES can provide physically plausible results when compared with experimental results (Roohi et al., 2013; Nourazar and Safavi, 2017; Huo et al., 2021).

5 Conclusions

In this study, we investigated the geometrical properties of the vapor cavity in the poppet-valve notch and the associated flow-choking phenomenon, using visualization experiments and LES numerical approaches. Two representative cases (face-sealing and line-sealing poppet valves) are used as examples to explain the formation of vortex-produced vapor cavities. In the face-sealing poppet valve, the internal vena contracta in the notch produces fixed local vortices and a fixed large-scale vapor cavity. In the line-sealing poppet valve, the external vena contracta downstream of the notch produces discrete vortices and discrete vapor cavities. We found that the distribution of vapor cavities is associated with the local low pressure caused by vortices, which differs significantly from the traditional perspective that the cavitation process always occurs at the throat of the notch with the highest velocity.

We also found that the properties of the vena contracta and vapor-cavity geometry are determined by the notch structure. The pressure condition only affects the number or scale of vapor cavities. The length-to-diameter ratio is determined by the valve opening, sealing length, and throttling angle, which are defined to measure the transition between internal and external vena contracta flow. For structures with larger R_a, the internal vena contracta dominates, leading to a stronger mass-transfer process from liquid to vapor in the fixed cavity and resulting in significant flow-choking. For structures with smaller R_a, the external vena contracta dominates, leading to a complete cavitation process in discrete vapor cavities and reducing flow-choking. The R_a threshold is estimated to be approximately 2.

Acknowledgments

This work is supported by the National Natural Science Foundation of China (Nos. 52075387 and 52375060), the Shanghai Natural Science Foundation of China (No. 22ZR1464400), the National Key R&D Program of China (No. 2019YFB2005102), the Shanghai Municipal Science and Technology Major Project (No. 2021SHZDZX0100), and the Fundamental Research Funds for the Central Universities (No. 2022-1-ZD-04), China.

Author contributions

Liang LU: conceptualization, writing–review & editing, supervision. Zhongdong LIANG: methodology, writing–original draft, writing–review & editing, formal analysis, investigation. Yuming LIU: formal analysis, investigation. Zhipeng WANG: supervision. Shohei RYU: resources.

Conflict of interest

Liang LU, Zhongdong LIANG, Yuming LIU, Zhipeng WANG, and Shohei RYU declare that they have no conflict of interest.

References

Altimira M, Fuchs L, 2015. Numerical investigation of throttle flow under cavitating conditions. *International Journal of Multiphase Flow*, 75:124-136. https://doi.org/10.1016/j.ijmultiphaseflow.2015.05.006

Brennen CE, 2014. Cavitation and Bubble Dynamics. Cambridge University Press, Cambridge, UK, p.10-22.

Chiavola O, Frattini E, Palmieri F, et al., 2019. Poppet valve performance under cavitating conditions. *AIP Conference Proceedings*, 2191(1):020045. https://doi.org/10.1063/1.5138778

Filo G, Lisowski E, Rajda J, 2021. Design and flow analysis of an adjustable check valve by means of CFD method. *Energies*, 14(8):2237. https://doi.org/10.3390/en14082237

Finnemore EJ, Franzini JB, 2002. Fluid Mechanics with Engineering Applications. 10th Edition. McGraw-Hill Education, New York, USA, p.505.

Gao Q, Zhu YC, Chen XM, et al., 2019. CFD simulation on flow field of a large flow rate high speed on/off valve. Proceedings of the 8th International Conference on Fluid Power and Mechatronics, p.224-230. https://doi.org/10.1109/FPM45753.2019.9035785

Gao Q, Zhu Y, Liu JH, 2022. Dynamics modelling and control of a novel fuel metering valve actuated by two binary-coded digital valve arrays. *Machines*, 10(1):55. https://doi.org/10.3390/machines10010055

Ghosal S, Moin P, 1995. The basic equations for the large eddy simulation of turbulent flows in complex geometry. *Journal of Computational Physics*, 118(1):24-37. https://doi.org/10.1006/jcph.1995.1077

Han MX, Liu YS, Wu DF, et al., 2017. A numerical investigation in characteristics of flow force under cavitation state inside the water hydraulic poppet valves. *International Journal of Heat and Mass Transfer*, 111:1-16. https://doi.org/10.1016/j.ijheatmasstransfer.2017.03.100

Hao QH, Wu WR, Tian GT, 2022. Study on reducing both flow force and cavitation in poppet valves. *Proceedings of the Institution of Mechanical Engineers, Part C: Journal of Mechanical Engineering Science*, 236(23):11160-11179.

https://doi.org/10.1177/09544062221110729

Hinze JO, 1975. Turbulence. McGraw-Hill, New York, USA.

Huo JL, Luan XY, Gong YW, et al., 2021. Numerical study of bund overtopping phenomena after a catastrophic tank failure using the axisymmetric approach. *Process Safety and Environmental Protection*, 153:464-471. https://doi.org/10.1016/j.psep.2021.07.044

Iravani M, Toghraie D, 2020. Design a high-pressure test system to investigate the performance characteristics of ball valves in a compressible choked flow. *Measurement*, 151: 107200. https://doi.org/10.1016/j.measurement.2019.107200

Kumagai K, Ryu S, Ota M, et al., 2016. Investigation of poppet valve vibration with cavitation. *International Journal of Fluid Power*, 17(1):15-24. https://doi.org/10.1080/14399776.2015.1115648

Li BB, Zhao Q, Li HY, et al., 2021. Analysis method of the cavitation vibration signals in poppet valve based on EEMD. *Advances in Mechanical Engineering*, 13(2): 1687814021998114. https://doi.org/10.1177/1687814021998114

Lu L, Zou J, Fu X, et al., 2009. Cavitating flow in non-circular opening spool valves with U-grooves. *Proceedings of the Institution of Mechanical Engineers, Part C: Journal of Mechanical Engineering Science*, 223(10):2297-2307. https://doi.org/10.1243/09544062JMES1504

Lu L, Xie SH, Yin YB, et al., 2020. Experimental and numerical analysis on the surge instability characteristics of the vortex flow produced large vapor cavity in u-shape notch spool valve. *International Journal of Heat and Mass Transfer*, 146:118882. https://doi.org/10.1016/j.ijheatmasstransfer.2019.118882

Lu L, Xu YP, Li MR, et al., 2022. Analysis of fretting wear behavior of unloading valve of gasoline direct injection high pressure pump. *Journal of Zhejiang University-SCIENCE A (Applied Physics & Engineering)*, 23:314-328. https://doi.org/10.1631/jzus.A2100685

Lu L, Wang J, Li MR, et al., 2022. Experimental and numerical analysis on vortex cavitation morphological characteristics in u-shape notch spool valve and the vortex cavitation coupled choked flow conditions. *International Journal of Heat and Mass Transfer*, 189:122707. https://doi.org/10.1016/j.ijheatmasstransfer.2022.122707

Manninen M, Taivassalo V, Kallio S, 1996. On the Mixture Model for Multiphase Flow. Technical Report No. VTT-PUB-288, Technical Research Centre of Finland, Espoo, Finland.

Martelli M, Gessi S, Massarotti GP, et al., 2017. On peculiar flow characteristics in hydraulic orifices. ASME/BATH Symposium on Fluid Power and Motion Control, Article V001T001A057. https://doi.org/10.1115/FPMC2017-4313

Min W, Wang HY, Zheng Z, et al., 2020. Visual experimental investigation on the stability of pressure regulating poppet valve. *Proceedings of the Institution of Mechanical Engineers, Part C: Journal of Mechanical Engineering Science*, 234(12):2329-2348. https://doi.org/10.1177/0954406220905872

Nicoud F, Ducros F, 1999. Subgrid-scale stress modelling based on the square of the velocity gradient tensor. *Flow, Turbulence and Combustion*, 62(3):183-200. https://doi.org/10.1023/A:1009995426001

Nourazar S, Safavi M, 2017. Two-dimensional large-eddy simulation of density-current flow propagating up a slope. *Journal of Hydraulic Engineering*, 143(9):04017035. https://doi.org/10.1061/(ASCE)HY.1943-7900.0001329

Pan M, Plummer A, 2018. Digital switched hydraulics. *Frontiers of Mechanical Engineering*, 13(2):225-231. https://doi.org/10.1007/s11465-018-0509-7

Roache PJ, 1998. Verification and Validation in Computational Science and Engineering. Hermosa Publishers, Albuquerque, USA.

Roohi E, Zahiri AP, Passandideh-Fard M, 2013. Numerical simulation of cavitation around a two-dimensional hydrofoil using VOF method and LES turbulence model. *Applied Mathematical Modelling*, 37(9):6469-6488. https://doi.org/10.1016/j.apm.2012.09.002

Schnerr GH, Sauer J, 2001. Physical and numerical modeling of unsteady cavitation dynamics. Proceedings of the 4th International Conference on Multiphase flow, p.1-12.

Singhal AK, Athavale MM, Li HY, et al., 2002. Mathematical basis and validation of the full cavitation model. *Journal of Fluids Engineering*, 124(3):617-624. https://doi.org/10.1115/1.1486223

Stosiak M, Skačkauskas P, Towarnicki K, et al., 2023. Analysis of the impact of vibrations on a micro-hydraulic valve using a modified induction algorithm. *Machines*, 11(2):184. https://doi.org/10.3390/machines11020184

Tamburrano P, Plummer AR, Distaso E, et al., 2019. A review of direct drive proportional electrohydraulic spool valves: industrial state-of-the-art and research advancements. *Journal of Dynamic Systems, Measurement, and Control*, 141(2): 020801. https://doi.org/10.1115/1.4041063

Wang S, Zhang B, Zhong Q, et al., 2017. Study on control performance of pilot high-speed switching valve. *Advances in Mechanical Engineering*, 9(7). https://doi.org/10.1177/1687814017708908

Yuan C, Song JC, Liu MH, 2019a. Investigation of flow dynamics and governing mechanism of choked flow for cavitating jet in a poppet valve. *International Journal of Heat and Mass Transfer*, 129:113-131. https://doi.org/10.1016/j.ijheatmasstransfer.2018.09.065

Yuan C, Song JC, Zhu LS, et al., 2019b. Numerical investigation on cavitating jet inside a poppet valve with special emphasis on cavitation-vortex interaction. *International Journal of Heat and Mass Transfer*, 141:1009-1024. https://doi.org/10.1016/j.ijheatmasstransfer.2019.06.105

Yuan C, Zhu LS, Liu SQ, et al., 2021. Examination of viscosity effect on cavitating flow inside poppet valves based on a numerical study. *Applied Sciences*, 11(23):11205. https://doi.org/10.3390/app112311205

Yuan C, Zhu LS, Liu SQ, et al., 2022. Numerical study on the cavitating flow through poppet valves concerning the influence of flow instability on cavitation dynamics. *Journal of Mechanical Science and Technology*, 36(2):761-773.

https://doi.org/10.1007/s12206-022-0124-8

Zhang JH, Wang D, Xu B, et al., 2018. Experimental and numerical investigation of flow forces in a seat valve using a damping sleeve with orifices. *Journal of Zhejiang University-SCIENCE A (Applied Physics & Engineering)*, 19(6):417-430.
https://doi.org/10.1631/jzus.A1700164

Zwart PJ, Gerber AG, Belamri T, 2004. A two-phase flow model for predicting cavitation dynamics. Proceedings of the 5th International Conference on Multiphase Flow, Article 152.

Electronic supplementary materials

Sections S1–S6